Fully-developed laminar flow in trapezoidal ducts with rounded corners: a numerical solution and case study

M.S. Ismail [a, b] [*], Mohamed R. Berber [c], Ziyad A. Alrowaili [d], M. Pourkashanian [a, b]

[a] Energy Institute, University of Sheffield, Sheffield S3 7RD, United Kingdom
[b] Translational Energy Research Centre (TERC), University of Sheffield, Sheffield S9 1ZA, United Kingdom
[c] Chemistry Department, College of Science, Jouf University, Sakaka 2014, Saudi Arabia
[d] Physics Department, College of Science, Jouf University, Sakaka 2014, Saudi Arabia

[*] Corresponding author: Tel: +44 114 21 57242
Email addresses: m.s.ismail@sheffield.ac.uk, msaeedaaal@gmail.com (M.S. Ismail)

Abstract

Purpose – This paper aims to numerically solve fully-developed laminar flow in trapezoidal ducts with rounded corners which result following forming processes.

Design/methodology/approach – A two-dimensional model for a trapezoidal duct with rounded corners is developed and conservation of momentum equation is solved. The flow is assumed to be steady, fully developed, laminar, isothermal and incompressible. The key flow characteristics including the Poiseuille number and the incremental pressure drop have been computed and tabulated for a wide range of: sidewall angle (θ); the ratio of the height of the duct to its smaller base (α); and the ratio of the fillet radius of the duct to its smaller base (β).

Findings – The results show that Poiseuille number decreases and all the other dimensionless numbers increase with increasing the radii of the fillets of the duct; these effects were found to amplify with decreasing duct heights or increasing sidewall angles. The maximum axial velocity was shown to increase with increasing the radii of the fillets of the duct. For normally-used ducts in hydrogen fuel cells, the impact of rounded corners cannot be overlooked for very low channel heights or very high sidewall angles.

Practical implications – The data generated in this study are highly valuable for engineers interested in estimating pressure drops in rounded trapezoidal ducts; these ducts have been increasingly used in hydrogen fuel cells where flow channels are stamped on thin metallic sheets.

Originality/value – Fully-developed laminar flow in trapezoidal ducts with four rounded corners has been solved for the first time, allowing for more accurate estimation of pressure drop.

1. Introduction

The polymer electrolyte fuel cell (PEFC) is a promising zero/low-emission power conversion technology; it has appealing features: high efficiency (~ 50%), low operating temperature (< 100°C) and subsequently rapid start-up (~ 1s) (Carcadea *et al.*, 2007; Hassan *et al.*, 2011). However, the PEFC technology has two main drawbacks that hinder its widespread deployment into the marketplace: high manufacturing cost and low durability (Neto *et al.*, 2019; Li and Sunden, 2018). To this end, there is an urgent need to innovate new material structures and/or designs to render the PEFC technology more commercially and technically competitive to the existing polluting power conversion technologies (Ismail *et al.*, 2016).

The bipolar plates (BPPs), also known as flow field plates, are key components in PEFCs. They simultaneously: supply the reactant gases (oxygen or hydrogen) flowing in their channels to the catalyst layers; electrically connect the cathode of one cell to the anode of the adjacent cell (hence the name bipolar plates); and assist in removing the excess liquid water from the membrane electrode assembly (MEA) of the fuel cell. BPPs have been traditionally made from high-density graphite as it is abundantly available and demonstrates high corrosion resistance (Karimi *et al.*, 2012). However, the graphitic BPPs are brittle and, therefore, require milling to create the flow channels, resulting in high manufacturing cost (Neto *et al.*, 2019). Therefore (and also bearing in mind that the BPPs accounts for about 30% of the total cost of the fuel cell stack (Kopasz and Benjamin, 2017)), there has been a trend towards using materials for BPPs for which the mass production is more cost-effective such as metals and polymer-carbon composites (Karimi *et al.*, 2012). Compared to composite BPPs, the metallic BPPs are mechanically stronger, more electrically conductive, and easier to be stamped and be substantially reduced in thickness (Karimi *et al.*, 2012; Liu and Hua, 2010). The main drawback of the metallic BPPs is that they have low corrosion resistance (Wang and Turner, 2010); if corroded, metallic BPPs release metal ions that contaminate the membrane electrolyte (Pozio

1   *et al.*, 2003). Furthermore, a passive film forms at the surface of the metallic BPPs which

2   subsequently increases the contact resistance between the BPP and the gas diffusion layer

3   (GDL) of the fuel cell (Neto *et al.*, 2019; Andre 2009). Therefore, metallic BPPs are normally

4   surface-treated with corrosion-resistant coatings to mitigate corrosion and the formation of the

5   passive film (Wlodarczyk *et al.*, 2016).

6   The flow channels in the metallic sheets are typically made using mass-production forming

7   processes such as stamping or hydroforming processes (Karimi *et al.,* 2012). As shown in

8   Figure 1, the channels of the stamped metallic sheets are, due to the requirements of forming

9   processes, typically trapezoidal with fillets, i.e. rounded corners (Xu *et al.,* 2016; Elyasi *et al.*

10   2017). The cross sections of the flow channels of the modelled PEFCs are often assumed to be

11   rectangular and this is due to the fact that such channels could be easily milled using graphitic

12   BPPs. If metallic sheets are used as BPPs for PEFCs, then the cross-sections of the channels in

13   these sheets are most likely to be trapezoidal; therefore, the flow characteristics (e.g. the

14   pressure drop, the maximum velocity and the hydrodynamic entrance length) are different to

15   those of the rectangular flow channel, thus potentially leading to significantly different

16   solutions of the fuel cell models. Trapezoidal channels are encountered in some engineering

17   devices such as compact heat exchanges, sensors and actuators (Renksizbulut and Niazmand,

18   2006) and there have been therefore some investigations on the hydrodynamic and heat

19   transfer-related characteristics of the flow within these channels. Below is a summary of the

20   key findings of these investigations.

21   **[Figure 1]**

22   Shah (1975) solved fully developed laminar flow and heat transfer in ducts with equilateral,

23   sine, rhombic and trapezoidal cross-sections by employing a discrete least squares method. For

24   trapezoidal ducts, the author computed and tabulated the flow and heat-transfer characteristics

25   for fully developed flow for a variety of sidewall angles and aspect ratios. Sadasivam *et al.*

1   (1999) solved fully developed laminar flow through trapezoidal and hexagonal ducts using a

2   finite difference method. They presented solutions for velocity and temperature distribution for

3   a wide range of duct aspect ratios and with four different sidewall angles. For each sidewall

4   angle (i.e. 30, 45, 60 or 75°), the Poiseuille numbers and the Nusselt numbers (with different

5   thermal boundary conditions) were presented as polynomial functions of the duct aspect ratio.

6   Flockhart and Dhariwal (1998) experimentally and numerically determined the flow

7   characteristics in etched-in-silicon trapezoidal micro-channels, with hydraulic diameters

8   ranging from 50 to 120 µm and a trapezoidal angle of around 55°. They concluded that the

9   numerical analysis, based on the continuum mechanics, could adequately predict the flow

10   characteristics of the trapezoidal micro-channels investigated in the study. Wu and Chang

11   (2003) arrived at the same conclusion: they stated that, comparing the experimental data they

12   obtained with those of the analytical solution developed by Ma and Peterson (1997), the

13   Navier-Stokes equations are valid for laminar flow of deionised water in smooth silicon

14   microchannels that have as small hydraulic dimeter as ~ 26 µm. McHale and Garimella (2010)

15   run three-dimensional simulations, using finite volume method (also known as control

16   volume), to investigate heat transfer in hydrodynamically fully developed and thermally

17   developing laminar flow in trapezoidal microchannels with a wide range of aspect ratio (0 to

18   100) and two sidewall angles: 45° and 54.7° which correspond to the etch-resistant planes in

19   the crystal structure of silicon. They introduced correlations for the local and average Nusselt

20   numbers as a function a dimensionless axial length variable. Further, for each sidewall angle,

21   they reported the fully developed Poiseuille and Nusselt numbers as a function of channel

22   aspect ratio.

23   Using a finite volume method, Farhanieh and Sunden (1991) analysed the developing laminar

24   flow and convective heat transfer in the entrance region of a trapezoidal duct and axially

25   constant wall temperature. They found that as the aspect ratio of the trapezoidal duct increases,

5

the incremental pressure drop increases and the heat transfer decreases. On the other hand, as the side wall angle increases, the heat transfer increases and the incremental pressure drop decreases. Similarly, Renksizbulut and Niazmand (2006) used finite volume method to solve the conservation equations of momentum and heat for a three-dimensional developing laminar flow in the entrance region of trapezoidal channels. They reported the same the effects of the aspect ratio and the sidewall angle on the heat transfer and the incremental pressure drop as Farhanieh and Sunden (1991). Interestingly, they showed that the axial velocity profiles develop overshoots in the regions close to the corners of the channels and these overshoots become more pronounced with decreasing sidewall angle (Renksizbulut and Niazmand, 2006). Yuan *et al.* (2001) numerically solved laminar flow and heat transfer for ducts with rectangular and trapezoidal cross sections with uniform mass injection/suction prescribed at one of the walls (mimicking the situation in real life fuel cells where fluids are consumed or generated at the surface of the electrode facing the flow channel). They found that, for all the geometries investigated, the Poiseuille number increases and Nusselt number decreases as the mass injection increases; opposite results were obtained with increasing mass suction.

Notably, Lorenzini and Morini (2011) solved fully developed laminar flow through rectangular and trapezoidal ducts with rounded corners using the least square method. They found that the increase in the Poiseuille and the Nusselt numbers of the rectangular ducts when rounding the corners is significantly higher than those of the trapezoidal ducts. However, they investigated the trapezoidal ducts with only two fillets which are the ones that connect the sides of the duct to its smaller base. As mentioned earlier in this introduction, the forming process of the metallic sheets typically result in trapezoidal ducts with all the corners being rounded (Xu *et al.* 2016; Elayasi *et al.* 2017); see Figure 2. It should be noted that, in these trapezoidal ducts, the centres of the two fillets between the sides of the duct and the smaller base are inside the duct whereas the centres of the fillets between the sides of the duct and the larger base are outside the duct.

1   To the best of authors' knowledge, the characteristics of fully-developed laminar flow in these

2   ducts have not been previously investigated. To this end, in this work, fully developed laminar

3   flow in trapezoidal flow ducts with four rounded corners (where the two corners connecting

4   the sidewalls to the smaller base of the duct are inwardly rounded and the two corners

5   connecting the sidewalls to the larger base of the duct are outwardly rounded) is solved for the

6   first time. The key flow characteristics (the Poiseuille number, the incremental pressure drop,

7   the dimensionless hydrodynamic entrance length and the ratio of the maximum axial velocity

8   to the mean axial velocity) were computed and tabulated for a wide range of sidewall angles,

9   the ratio of duct height to its smaller base and the ratio of the fillet radius of the duct to its

10   smaller base. The sensitivity of the velocity profile across the duct to the roundness of the

11   corners of the duct was also investigated. Putting theory into practice, the pressure drop and

12   other important properties (i.e. the hydrodynamic entrance length and the maximum axial

13   velocity) were calculated for polymer electrolyte fuel cell trapezoidal flow ducts with

14   sharp/rounded corners to evaluate the effects of the 'roundness' of the corners on all the

15   abovementioned flow properties.

16   **2. Problem Formulation**

17   A steady, fully developed, laminar, isothermal and two-dimensional flow of an incompressible

18   Newtonian fluid is considered. The fluid flows in a trapezoidal ducts with rounded corners

19   (Figure 2); the symbols displayed at the cross-section represent the following: the height of the

20   duct (h), the smaller base of the duct (a), the radius of the fillet (r) and the sidewall angle (θ).

21   α is the ratio of the height of the duct to its smaller base and β is the ratio of the radius of the

22   fillet of the duct to its smaller base.

23   **[Figure 2]**

1 The flow is fully developed and therefore the continuity equation is satisfied automatically.

2 With all the above considerations, the conservation of momentum equation reduces to

3 Poisson's equation:

$$\frac{\partial^2 u}{\partial x^2} + \frac{\partial^2 u}{\partial y^2} = \frac{1}{\mu}\frac{dP}{dz} \tag{1}$$

4 where u is the axial velocity (i.e. the velocity in the direction of the flow), P is the pressure and

5 μ is the fluid viscosity. Note that the right hand side of Equation (1) (i.e. $\frac{1}{\mu}\frac{dP}{dz}$) is treated as a

6 constant. Due to the symmetry, only half of the cross-section of the trapezoidal channel was

7 modelled; see Figure 3. The boundary conditions used to solve Equation (1) are the no-slip

8 boundary condition at the perimeter of the modelled geometry (Γ) and zero flux at the

9 centreline of the modelled geometry; see Figure 3.

10 **[Figure 3]**

11 Once the solution of velocity field is obtained, a number of dimensionless numbers are used to

12 characterise the flow in the duct. One of the dimensionless number that is normally used for

13 the pressure drop calculations of the fully developed flow is the Poiseuille number or fRe,

14 which is the product of the Fanning friction factor f and the Reynolds number Re:

$$f = \frac{1}{2}\frac{D_h}{\rho u_m^2}\frac{\Delta P}{L} \tag{2}$$

$$Re = \frac{\rho u_m D_h}{\mu} \tag{3}$$

15 where L is the distance along which the pressure drops, u_m is the mean axial velocity and ρ is

16 the density of the fluid. D_h is the hydraulic diameter of the channel and is typically defined as:

$$D_h = \frac{4A}{\Gamma} \tag{4}$$

1   where A is the cross section of the channel and Γ is the wetted perimeter of the channel. The

2   incremental pressure drop, $K(\infty)$, the dimensionless hydrodynamic entrance length, L_{hy}^* and

3   the ratio of the maximum axial velocity to the mean axial velocity (u_{max}/u_m) are three more

4   key flow parameters. The knowledge of fRe and $K(\infty)$ allows for the estimation of the total

5   pressure drop that is made up from the pressure drop associated with the developing flow region

6   (i.e. the hydrodynamic entrance length) and the pressure drop associated with the fully

7   developed region (Shah and London, 1978):

$$\frac{\Delta P}{\rho\, u_m^2/2} = fRe\,\frac{4L}{D_h Re} + K(\infty) \tag{5}$$

8   $K(\infty)$ is obtained as follows (Shah, 1975; Farhanieh and Sunden, 1991):

$$K(\infty) \;=\; 2[K_e(\infty) - K_d(\infty)] \tag{6}$$

9   where $K_e(\infty)$ is the kinetic energy correction factor:

$$K_e(\infty) = \frac{1}{A}\int \left(\frac{u}{u_m}\right)^3 dA \tag{7}$$

10   and $K_d(\infty)$ is the momentum flux correction factor:

$$K_d(\infty) = \frac{1}{A}\int \left(\frac{u}{u_m}\right)^2 dA \tag{8}$$

11   The dimensionless hydrodynamic entrance length (L_{hy}^*) requires the knowledge of all the other

12   three dimensionless numbers $(fRe, K(\infty)$ and $u_{max}/u_m)$ (Shah and London, 1978):

$$L_{hy}^* = \frac{(u_{max}/u_m) - 1 - K(\infty)}{4fRe} \tag{9}$$

13   The knowledge of L_{hy}^* allows for the calculation of hydrodynamic entrance length (L_{hy}) (Shah,

14   1975):

$$L_{hy} \;=\; L_{hy}^* D_h Re \tag{10}$$

15   **3. Solution Procedure**

9

1 The two-dimensional domain was discretised and the governing equation, Equation (1), was

2 solved using finite element analysis software, COMSOL Multiphysics®. Unstructured free

3 triangular elements were used to discretise the geometries. Figure 4 shows a meshed geometry

4 for a trapezoidal cross-section with a sidewall angle (θ) of 60°, a height to small base ratio (α)

5 of 1.0 and a fillet radius to small base ratio (β) of 0.5. It is noteworthy that the geometry has a

6 sharp edge at its lower base which normally requires a much finer mesh to obtain a more

7 accurate solution. So we initially applied a very refined fine mesh in the vicinity of the sharp

8 edge. However, there was almost insignificant gain in precision of solution performing the

9 above exercise. Therefore, the time-saving and automatically-generated meshing scheme was

10 considered for the computation cases. Table 1 shows the change in the computed fRe with the

11 mesh size. It shows that the computed fRe starts to be accurate to 3 decimal places with the

12 300 elements. However, as the computation time was not an issue (< 5 seconds), a mesh that

13 achieves a 5 decimal places accuracy (e.g. ~ 2900 elements for this case) was selected for all

14 the computational cases.

15 **[Figure 4 and Table 1]**

16 **4. Results and Discussion**

17 Figure 5 shows the computed fRe, $K(\infty)$, L_{hy}^* and u_{max}/u_m as functions of α for a variety of

18 θ (i.e. 30, 45, 60, 75 and 85°); the figures shows that the obtained results are in excellent

19 agreement with the well-known data reported by Shah (Shah, 1975); the numerical values of

20 the two sets of data (i.e. Shah's data and our data) have at least the same 2 decimal places. Note

21 that the results shown in Figure 5 are for trapezoidal ducts with sharp corners (i.e. $\beta = 0$). To

22 the best of authors' knowledge, there have been no similar results for trapezoidal ducts with

23 rounded corners (i.e. $\beta > 0$). The graphs in Figure 5 reveal two interesting trends that worth

24 spotlighting: (i) for relatively low sidewall angles ($\leq$ 60°) and high α (> 2), all the

25 dimensionless numbers approach a plateau with increasing α and (ii) the curves for the

10

1   dimensionless numbers $K(\infty)$, L_{hy}^* and u_{max}/u_m demonstrate similar trends to each other;

2   however, these trends are almost completely opposite to the trend demonstrated by the fRe

3   curve.

4   **[Figure 5]**

5   Having validated the model, the model was then solved for different combinations of θ, α

6   and β and the key flow dimensionless numbers were computed. Namely, Table 2 lists the

7   computed values for fRe, $K(\infty)$, L_{hy}^* and u_{max}/u_m for different values of θ (90, 75, 60, 45

8   and 30°), α (0.5, 1 and 2) and β (0, 0.1, 0.2, 0.3, 0.4 and 0.5). It could be seen from the table

9   that, for given θ and α, fRe decreases with increasing β and all of the other dimensionless

10   numbers (i.e. $K(\infty)$, L_{hy}^* and u_{max}/u_m) increase with increasing β. Also, one could note that

11   the impact of β on all the above dimensionless numbers becomes more pronounced with

12   decreasing α or increasing θ. Note that only three β values (0, 0.1 and 0.2) were used for the

13   cases in which θ is 75 and 90°. This is due to the fact that the distance between the upper and

14   lower corners for these two angels are not sufficiently large to significantly round the corners

15   ($\beta \geq 0.3$). We next explore the effect of the rounded corners (and the interplay between them

16   and both α and θ) on the velocity profiles across the duct.

17   **[Table 2]**

18   Figure 6 shows the dimensionless (i.e. the local velocities divided by the mean axial velocity)

19   iso-velocity profiles across trapezoidal ducts for different β (0, 0.1, 0.2, 0.3, 0.4 and 0.5) values

20   for an α of unity and a sidewall angle of 60°. The figure shows that the maximum velocity

21   slightly increases and that the flow is squeezed more towards the centre of the duct as β

22   increases; this is attributed to the increased 'sharpness' of the lower corner that slightly

23   increases the velocity gradients near to the wall of the duct and subsequently pushes the

24   momentum further towards the centre of the duct.

11

1 Figure 7 shows the velocity profiles for different α (0.5, 1 and 2) for a given θ (60°) and two

2 β values: zero (sharp corners) and 0.5. It can be seen from these profiles that the impact of β

3 becomes more pronounced as the aspect ratio α decreases. For example, for a given α of 0.5,

4 the maximum dimensionless iso-velocity increases from 1.87 to 1.97 when switching from

5 sharp ($\beta = 0$) to rounded corners ($\beta = 0.5$). This should be compared with the cases in which

6 α is 2; the maximum dimensionless iso-velocity only increases from 2.05 to 2.06 when

7 switching from sharp to rounded corners. This is evidently due to the fact that the 'squeezed'

8 geometry ($\alpha = 0.5$) allows for the impact of the lower rounded corner (in terms of pushing

9 momentum towards the centre of the duct) to become more pronounced compared to other

10 cases ($\alpha = 1$ or 2). As a general note, for either sharp or rounded corners, the velocity gradients

11 close to the walls increases and the flow therefore becomes more 'conical' as the aspect ratio

12 α increases; this is in line with the relevant results reported in (Sadasivam *et al.*, 1999).

13 Figure 8 shows the velocity profiles for three different sidewall angels (45, 60 and 75°), a single

14 aspect ratio α of unity and two β values: zero and 0.5. The profiles show that the effect of β

15 becomes slightly stronger as θ increases. As θ increases, the geometry, for a given α, become

16 more 'compact', thus allowing the lower rounded corners of the duct to push momentum

17 towards the core region of the duct. Further, it is noteworthy that, for either sharp or rounded

18 corners, the velocity gradients near to the walls of the duct increases as θ decrease, thus

19 resulting in a more 'conical' flow and increased maximum velocity.

20 **[Figures 6, 7 and 8]**

21 **Case study**

22 In this case study, we demonstrate how the dimensionless numbers computed in this work

23 (fRe, $K(\infty)$, L_{hy}^* and u_{max}/u_m) are used to estimate the pressure drop (ΔP), the hydrodynamic

24 entrance length (L_{hy}) and the maximum axial velocity (u_{max}) in a polymer electrolyte fuel cell

25 flow channel. As mentioned in the introduction, the metallic bipolar plates (which have been

1 increasingly used in PEFCs) are typically mass-produced through forming processes which

2 normally result is trapezoidal channels with rounded corners. It is therefore of interest to

3 evaluate the effects of the rounded corners of the trapezoidal channels on the key characteristics

4 of the fluid flow: ΔP, L_{hy} and u_{max}. Let us assume that the fuel cell in question has bipolar

5 plates that are of the commonly-used serpentine flow configuration (see the top view of the

6 schematic shown in Figure 9) and it generates 50 A electric current. Using Faraday's second

7 law of electrolysis, this amount of electric current requires provision of around 0.9 litre/min air

8 flow rate to the cathode side of the fuel cell and around 0.4 litre/min hydrogen fuel to the anode

9 side of the fuel cell. These calculated flow rates are practically increased a by factor of 1.5 to

10 2; the latter factor was selected for both gases. Table 3 shows the geometrical and the physical

11 properties used to determine the dimensionless numbers. It can be seen from this table that the

12 ratio α (h/a) is 1 and the ratio β (r/a) is either 0 (sharp corners) or 0.5 (rounded corners).

13 **[Figure 9 and Table 3]**

14 The dimensionless numbers (fRe, $K(\infty)$, L_{hy}^* and u_{max}/u_m) are subsequently obtained from

15 Table 2 for the cases in which α is 1, θ is 60° and β is either 0 or 0.5; see Table 4. Table 4 also

16 shows the Reynolds numbers, and the parameters used to calculate them (i.e. u_m and D_h along

17 with the physical properties of the flowing fluids listed in Table 3), for the cathodic and the

18 anodic flow channels with sharp ($\beta = 0$) or rounded ($\beta = 0.5$) corners. Note that the hydraulic

19 diameter of the channel with the rounded corners is smaller than that with the sharp corners

20 and this is due to the increased perimeter of the channel in the former case. It is also noteworthy

21 that the Reynolds numbers calculated for all the four sharp and the rounded cathodic and anodic

22 flow channels are less than 2300, signifying that the flows in all these channels are laminar.

23 **[Table 4]**

24 The pressure drop and the hydrodynamic entrance length for the various cases were, making

25 use of the data shown in Table 4, calculated using Equations (5) and (10) respectively; see

13

1   Table 5. The maximum axial velocity was calculated (and listed in Table 5) from the knowledge

2   of the mean axial velocity shown in Table 4 and the ratio u_{max}/u_m. The table also displays

3   the breakdown of the pressure drop into the pressure drop associated with the fully developed

4   flow region (ΔP_{fd}), which is the first term in Equation (5) multiplied by $\rho\, u_m^2/2$, and the

5   pressure drop associated with the developing flow region (ΔP_{df}), which is the second term in

6   Equation (5) multiplied by $\rho\, u_m^2/2$. It should be noted that the length of the channel (L in

7   Equation (5)) was set to be 3 m. This value was based on the assumption that active area of the

8   fuel cell is square and is 100 mm × 100 mm and that the spacing between the two consecutive

9   long straight segments (see Figure 9) is either 1 mm (for $\beta = 0$) or 0.5 mm (for $\beta = 0.5$). The

10   spacing in the latter case is smaller as the large base of the channel become larger when

11   switching from $\beta = 0$ to $\beta = 0.5$. To this end, the number of long straight segments of the

12   channel is 30 and the length of the channel is subsequently 30 × 100 mm (3 m). For simplicity,

13   the short straight segments connecting the long straight segments and the bends were not taken

14   into account when performing the pressure drop calculations; therefore, the total pressure drop

15   values shown in Table 5 are underestimated. Three-dimensional numerical simulations for one

16   U-turn of the flow channel were run (not shown) and showed that the total pressure drop is

17   underestimated by around 40% if the bends and the short segments are not accounted for.

18   However, this underestimation applies to both cases (i.e. $\beta = 0$ to $\beta = 0.5$) and it therefore does

19   not have an impact on the trends obtained in relation to the effects of the rounded corners.

20   The results show that, for either the cathode or the anode side of the fuel cell, the pressure drop

21   slightly increases (~ 3%) when switching from sharp ($\beta = 0$) to rounded corners ($\beta = 0.5$). This

22   increase is predominantly associated with the pressure drop associated with the fully-developed

23   region of the channel (ΔP_{fd}); the contribution of the pressure drop in the developing flow

24   region (ΔP_{df}) to the total pressure drop is almost negligible (< 0.1%). These results should be

25   dealt with carefully as the impact of β on the pressure drop may, depending on other

1   geometrical parameters, become much more significant. For example, if the height of the

2   channel (h) is decreased from 1 to 0.5 mm, then the increase in pressure drop as a result of

3   switching from sharp to rounded corners will be significantly higher: ~ 8% (not shown). As a

4   general note, the pressure drop in the anodic flow channels is significantly lower than that in

5   the cathodic flow channel and this is evidently due to extremely low density of hydrogen (see

6   Table 3) and lower flow rate used for the anode side of the fuel cell.

7   The roundness of the corners of the channels have almost no impact on the hydrodynamic

8   entrance length of the channel (L_{hy}): L_{hy} very slightly decreases (< 1%) when switching from

9   sharp to rounded corners. Owing to the same reasons mentioned for the pressure drop results,

10 the hydrodynamic entrance length in the anodic flow channel is significantly lower than that in

11 the cathodic flow channel. On the other hand, the maximum axial velocity (u_{max}) increases

12 very slightly (~ 1%) when switching from sharp to rounded corners; this is in accordance with

13 the trends demonstrated by the iso-velocity profiles shown in Figure 6, Figure 7 and Figure 8

14 where the presence of rounded corners (or the increase in the degree of the corner roundness)

15 was found to increase the maximum axial velocity. As a general note, the maximum

16 hydrodynamic entrance length was found to be less than 2% of the total length of the flow

17 channel (3 m), signalling that the fully developed flow significantly prevails over the

18 developing flow associated with the hydrodynamic entrance length. Finally, it is probably of

19 interest to the readers to appreciate the impact of the roundness of the corners of the trapezoidal

20 ducts on the performance of the fuel cell. Therefore, we have created a three-dimensional model

21 for a portion of PEFC incorporating the cathodic and the anodic flow channels (not shown).

22 The outputs of this model shows that the current density for a given operating cell potential

23 decreases by around 10% (at 0.7 V) to 20% (at 0.5 V) when switching from sharp ($\beta = 0$) to

24 rounded corners ($\beta = 0.5$). This is, corroborated by the dimensionless iso-velocity profiles

25 shown in Fig. 6, 7 and 8, attributed to the observation that the size of the dead zones (mainly

15

located within the vicinity of the corners adjacent to the surface of the gas diffusion layers) is higher with rounded corners ($\beta = 0.5$) than with sharp corners ($\beta = 0$), thus resulting in less reacting gases supplied to the catalyst layers of the fuel cell. Note that this model has not been shown and described in the paper as it would considerably increase its size and it may divert the attention from the main focus of the paper which is to compute the characteristics of fully-developed laminar flow in trapezoidal ducts with rounded corners that could be used for any application involving such ducts. However, this three-dimensional PEFC model forms an excellent skeleton for a potentially future work.

[Table 5]

5. Conclusions

Fully-developed laminar flow in trapezoidal ducts with four rounded corners has been numerically solved. The key flow characteristics in terms of the Poiseuille number (fRe), the incremental pressure drop ($K(\infty)$), the dimensionless hydrodynamic entrance length (L_{hy}^*) and the ratio of the maximum axial velocity to the mean axial velocity (u_{max}/u_m) have been computed and tabulated for a wide range of the sidewall angle (θ), the height of the duct to its small base ratio (α) and the radius of the fillet of the duct to its small base ratio (β). The effects of the rounded corners on the velocity profiles across the duct have been also investigated. A case study in which the impact of the rounded corners of a real-life hydrogen fuel cell trapezoidal flow channel on the pressure drop, the hydrodynamic entrance length and the maximum axial velocity has been introduced. The following are the key findings of the study:

- The Poiseuille number fRe decreases with increasing the radii of the fillets of the duct while the other dimensionless numbers ($K(\infty)$, L_{hy}^* and u_{max}/u_m) increase with increasing the radii of the fillet of the duct. These effects become more profound as the duct height decreases or sidewall angle increases.

16

1   •   The maximum axial velocity across the duct increases with increasing the radii of the fillets

2   of the duct. This is due to the corresponding increased velocity gradients near to the wall

3   of the duct that pushes the momentum towards the core of the duct. These effects amplify

4   as α decreases or θ increases.

5   •   The case study (in which typical values for α and θ were used for a hydrogen fuel cell

6   trapezoidal flow channel) shows that the highly rounded corners ($\beta = 0.5$), compared to

7   the sharp corners ($\beta = 0$), slightly increase the pressure drop and the maximum axial

8   velocity, and slightly decrease the hydrodynamic entrance length of the channel. It is

9   therefore appropriately safe for this particular case not to account for the rounded corners

10   in the modelled fuel cell. However, such an impact cannot be overlooked for very low

11   channel heights (very low α) or very high sidewall angles.

12 **Nomenclature**

A	*Duct cross-sectional area (m^2)*
a	*Duct small base (m)*
D_h	*Hydraulic diameter (m)*
fRe	*Poiseuille number*
f	*Fanning friction factor*
h	*Duct height (m)*
$K_d(\infty)$	*Momentum flux correction factor*
$K_e(\infty)$	*Kinetic energy correction factor*
$K(\infty)$	*Incremental pressure drop*
L_{hy}^*	*Dimensionless hydrodynamic entrance length*
L_{hy}	*Hydrodynamic entrance length (m)*
P	*Pressure (Pa)*
Re	*Reynolds number*
r	*Radius of fillet of duct (m)*
u_m	*Mean axial velocity (m s^{-1})*

17

u_{max}	*Maximum axial velocity (m s^{-1})*
u	*Axial velocity (m s^{-1})*
x, y, z	*Cartesian coordinates*
Γ	*Duct perimeter (m)*
α	*Ratio of h to a*
β	*Ratio of r to a*
θ	*Sidewall angle (°)*
μ	*Viscosity (Pa s)*
ρ	*Density (kg m^{-3})*

Subscripts

hy	*Hydrodynamic*
df	*Developing flow*
fd	*Fully developed*

1

References

3   Andre, J., Antoni, L., Petit, J.P., Vito, E.D., Montani, A. (2009), "Electrical contact resistance

4   between stainless steel bipolar plate and carbon felt in PEFC: A comprehensive study",

5   International Journal of Hydrogen Energy, Vol. 34 No. 7, pp. 3125-3133.

6   Carcadea, E., Ene, H., Ingham, D.B., Lazar, R., Ma, L., Pourkashanian, M. and Stefanescu, I.

7   (2007), "A computational fluid dynamics analysis of a PEM fuel cell system for power

8   generation", International Journal of Numerical Methods for Heat & Fluid Flow, Vol. 17

9   No. 3, pp. 302-312.

10   Elyasi, M., Khatir, F.A., Hosseinzadeh, M. (2017), "Manufacturing metallic bipolar plate fuel

11   cells through rubber pad forming process", The International Journal of Advanced

12   Manufacturing Technology, Vol. 89, pp. 3257-3269.

18

Farhanieh, B., Sunden, B. (1991), "Three-dimensional Laminar Flow and Heat Transfer in the Entrance Region of Trapezoidal Ducts", International Journal for Numerical Methods in Fluids, Vol. 13, pp. 537-556.

Flockhart, S.M., Dhariwal, R.S. (1998), "Experimental and Numerical Investigation into the Flow Characteristics of Channels Etched in <100> Silicon", Journal of Fluids Engineering, Vol. 120, pp. 291-295.

Hasan, A.B.M., Wahab, M.A. and Guo, S.M. (2011), "CFD analysis of a PEM fuel cell for liquid dispersion at the interface of GDL-GFC", International Journal of Numerical Methods for Heat & Fluid Flow, Vol. 21 No. 7, pp. 810-821.

Ismail, M., Ingham, D., Hughes, K.J., Ma, L. and Pourkashanian, M. (2016), "The effects of shape on the performance of cathode catalyst agglomerates in polymer electrolyte fuel cells", International Journal of Numerical Methods for Heat and Fluid Flow, Vol. 26 Nos 3/4, pp. 1145-1156.

Karimi, S., Fraser, N., Roberts, B., Foulkes, F.R. (2012), "A Review of Metallic Bipolar Plates for Proton Exchange Membrane Fuel Cells: Materials and Fabrication Methods", Advances in Materials Science and Engineering, No 828070, pp. 1-22.

Kopasz, J.P., Benjamin, T.G. (2017), "2017 Bipolar Plate Workshop Report", Argonne national Laboratory.

Li, S. and Ake Sunden, B. (2018), "Numerical analysis on thermal performance of cooling plates with wavy channels in PEM fuel cells", International Journal of Numerical Methods for Heat and Fluid Flow, Vol. 28 No. 7, pp. 1684-1697.

Liu, Y., Hua, L. (2010), "Fabrication of metallic bipolar plate for proton exchange membrane fuel cells by rubber pas forming", Journal of Power Sources, Vol. 195 No. 11, pp. 3529-3535.

Lorenzini, M., and Morini G.L. (2011), "Single-Phase Laminar Forced Convection in Microchannels With Rounded Corners", Heat Transfer Engineering, Vol. 32 No. 13-14, pp. 1108-1116.

Ma, H.B., Peterson, G.P. (1997), "Laminar Friction Factors in Microscale Ducts of Irregular Cross Section", Microscale Thermophysical Engineering, Vol. 1 No. 3, pp. 253-265.

McHale, J.P., Garimella, S.V. (2010), "Heat transfer in trapezoidal microchannels of various aspect ratios", International Journal of Heat and Mass Transfer, Vol. 53 No. 1-3, pp. 365-375.

Neto, D.M., Oliveria, M.C., Alves, J.L., Menezes, L.F. (2019), "Numerical Study on the Formability of Metallic Bipolar Plates for Proton Exchange Membrane (PEM) Fuel Cells", Metals, Vol. 9 No. 810, pp. 1-22.

Pozio, A., Silva, R.F., Francesco, M.D., Giorgi, L. (2003), "Nafion degradation in PEFCs from end plate iron contamination", Electrochimica Acta, Vol. 48 No 11, pp. 1543-1549.

Renksizbulut, M., Niazmand, H. (2006), "Laminar Flow and Heat Transfer in the Entrance Region of Trapezoidal Channels with Constant Wall Temperature", Journal of Heat Transfer, Vol. 128 No. 1, pp. 63-74.

Sadasivam, R., Manglik, R.M., Jog, M.A. (1999), "Fully developed forced convection through trapezoidal and hexagonal ducts", International Journal of Heat and Mass Transfer, Vol. 42 No. 23, pp. 4321-4331.

Shah, R.K. (1975), "Laminar Flow and Forced Convection Heat Transfer in Ducts of Arbitrary Geometry", International Journal of Heat and Mass Transfer, Vol. 18 No. 7-8, pp. 849-862.

Shah, R.K., London, A.L. (1978), "Laminar Flow Forced Convection in Ducts", Academic Press & Sons, New York, US.

1   Wang, H., Turner, J.A. (2010), "Reviewing Metallic Bipolar Plates", Fuel Cells, Vol. 10 No.

2   4, pp. 510-519.

3   Wlodarczyk, R., Zasada, D., Morel, S., Kacprzak, A. (2016), "A comparison of nickel coated

4   and uncoated sintered stainless steel used as bipolar plates in low-temperature fuel cells",

5   International Journal of Hydrogen Energy, Vol. 41 No. 39, pp. 17644-17651.

6   Wu, H.Y., Cheng, P. (2003), "Frictions factors in smooth trapezoidal silicon microchannels

7   with different aspect ratio", International Journal of Heat and Mass Transfer, Vol. 46 No.

8   14, pp. 2519-2525.

9   Xu, Y., Peng, L., Yi, P., Lai, X. (2016), "Analysis of the flow distribution for this stamped

10   bipolar plates with tapered channel shape", International Journal of Hydrogen Energy, Vol.

11   41 No 9, pp. 5084-5095.

12   Yuan, J., Rokni, M., Sunden, B. (2001), "Simulation of fully developed laminar heat and mass

13   transfer in fuel cell ducts with different cross-sections", International Journal of Heat and

14   Mass Transfer, Vol. 44 No. 21, pp. 4047-4058.

15

1

2

3

4

5

6

7

8

9

Flow Channel

Membrane
Electrode
Assembly

10
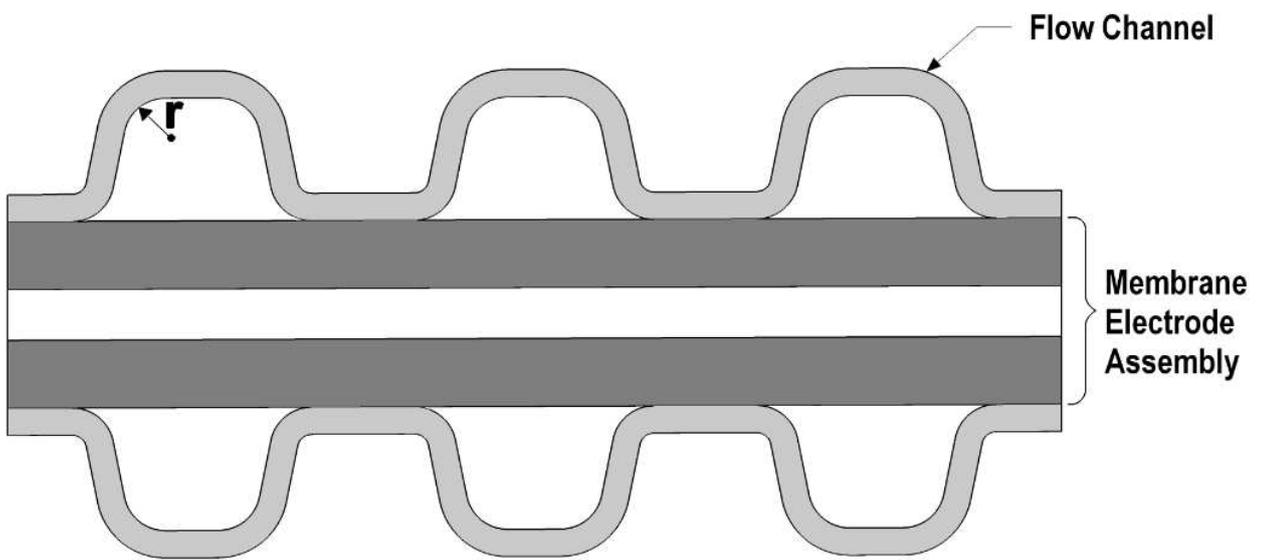
Figure 1 A typical cross-section of a fuel cell with stamped metallic sheet BPPs.

12

13

1

2

3

4

5

6

7

8

9

$$\alpha = h/a$$
$$\beta = r/a$$

10
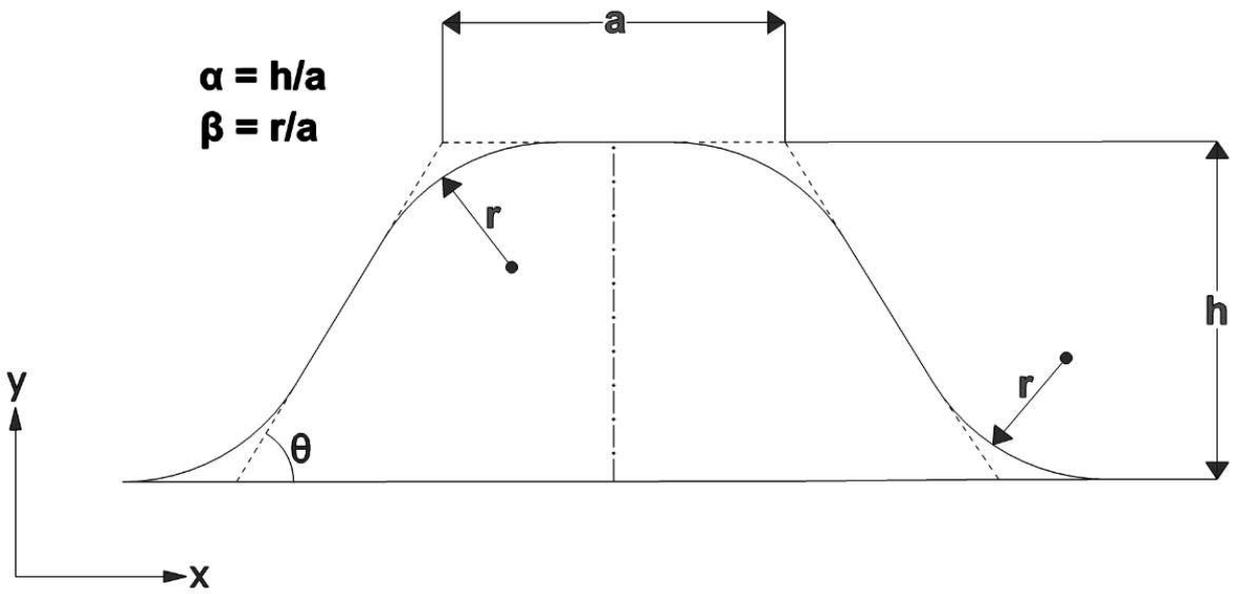
Figure 2 A cross-section for a trapezoidal duct with rounded corners.

12

13

14

1

2

3

4

5

6

7

8

9

$$\partial u/\partial n = 0$$

$$u(\Gamma) = 0$$

y

$$u(\Gamma) = 0$$

X

10
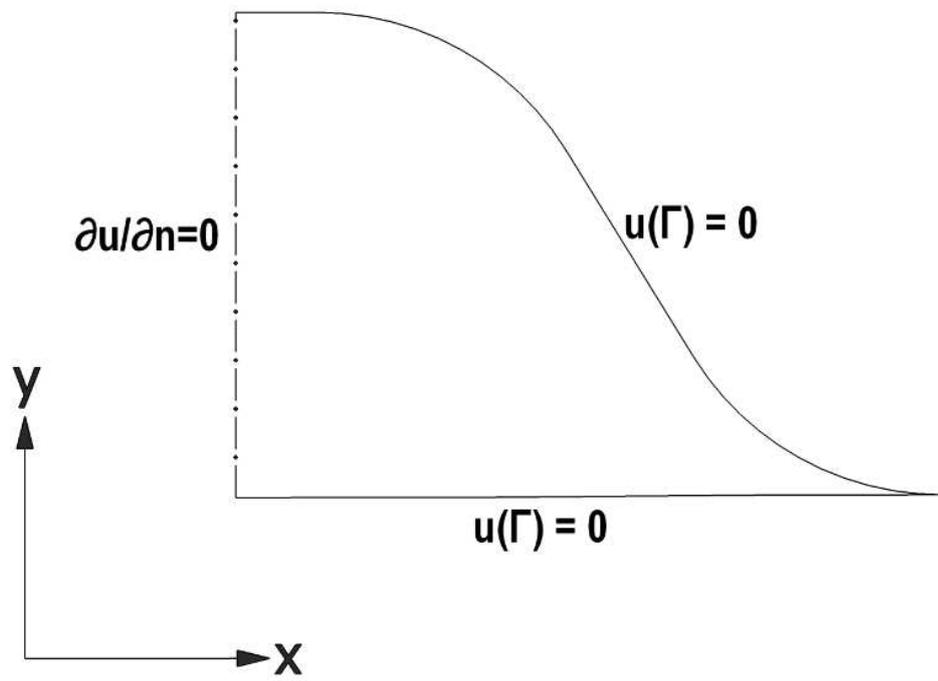
11   **Figure 3 The modelled geometry labelled with the boundary conditions.**

12

13

14

15

1

2

3

4

5

6

7

8
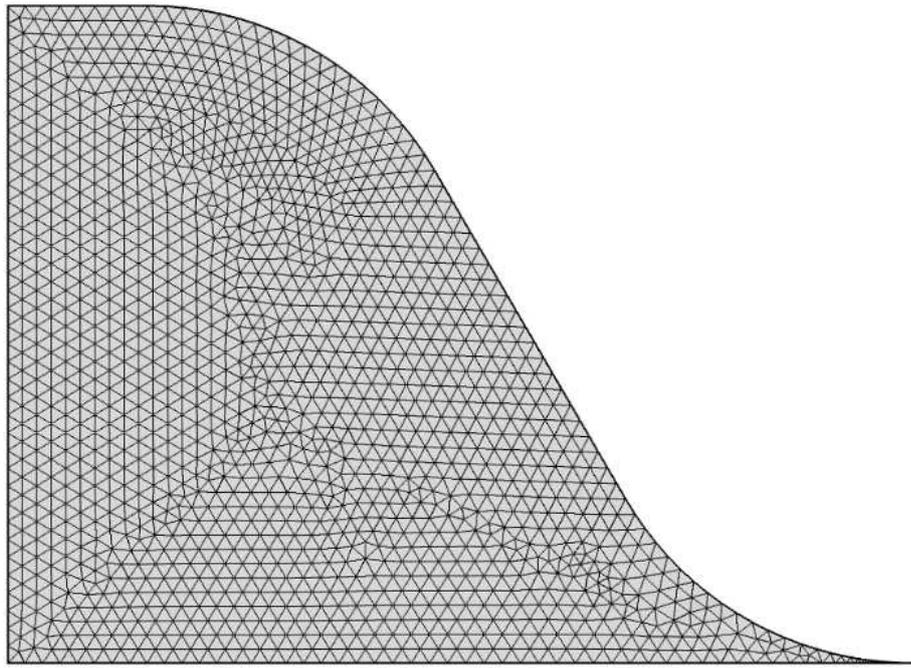
Figure 4 A meshed geometry for a trapezoidal cross-section with the following parameters: $\alpha = 1$, $\beta = 0.5$ and $\theta = 60$ °. The number of elements for this mesh is around 2900.

12

13

14

15

16

1

2

3

4

5

(a)

(b)

(c)

(d)

6
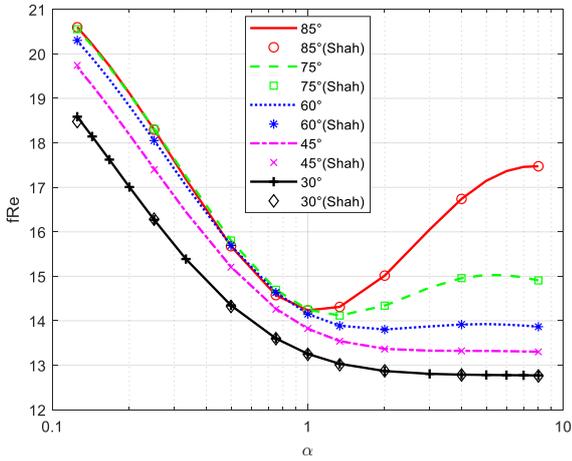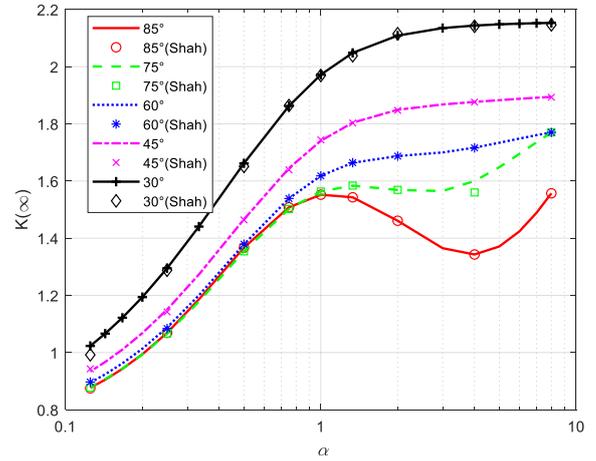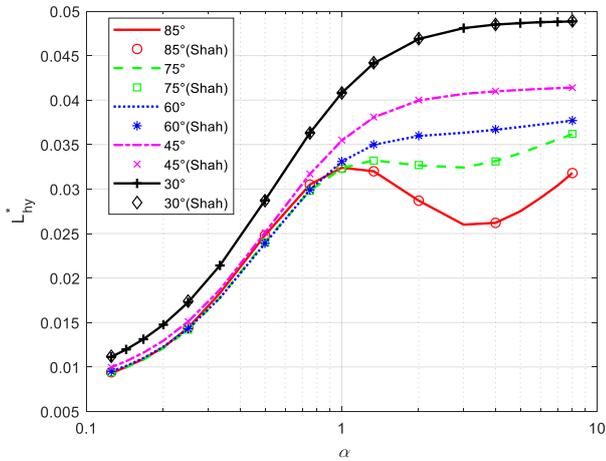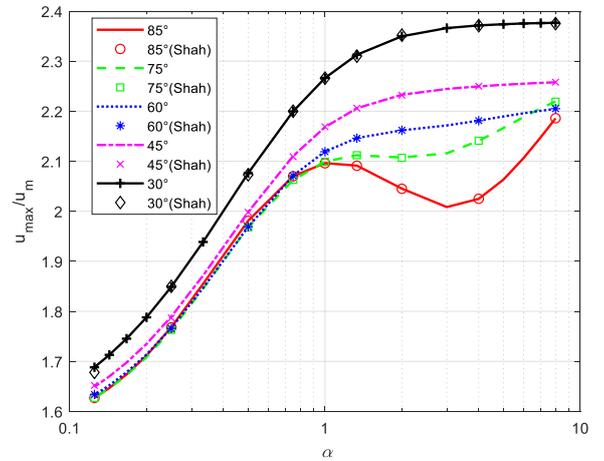
7   **Figure 5 Variation of (a) fRe, (b) K(∞), (c) L$_{hy}^{*}$ and (d) u$_{max}$/u$_m$ with α of**

8   **trapezoidal ducts that have sharp corners ($\beta = 0$).**

9

10

11

26

β = 0.0

β = 0.1

β = 0.2

β = 0.3

β = 0.4
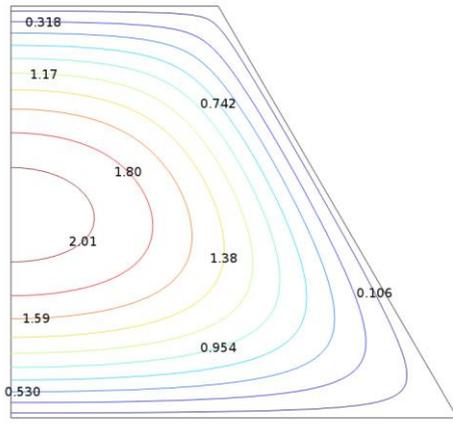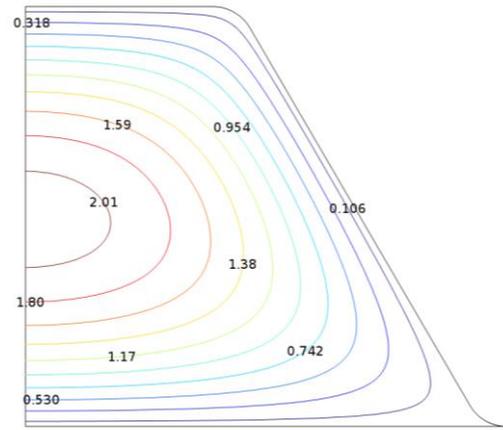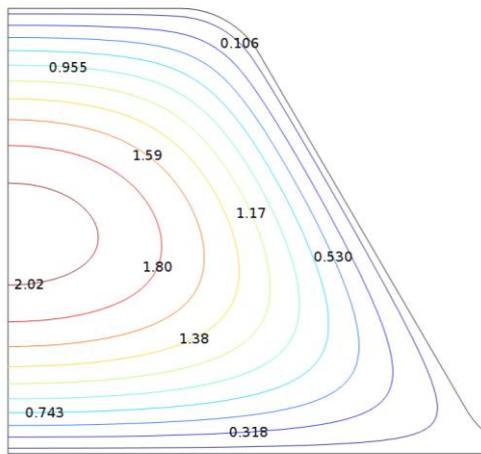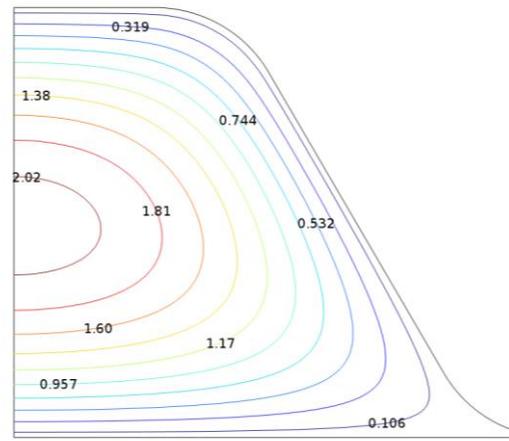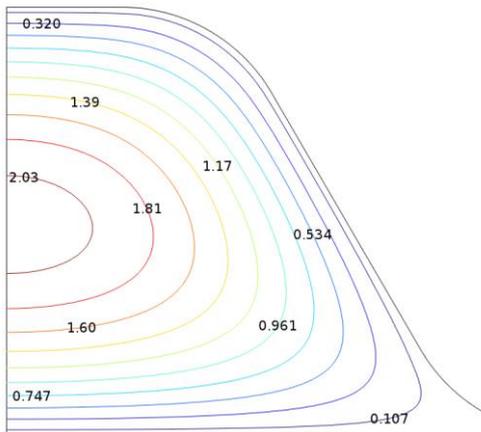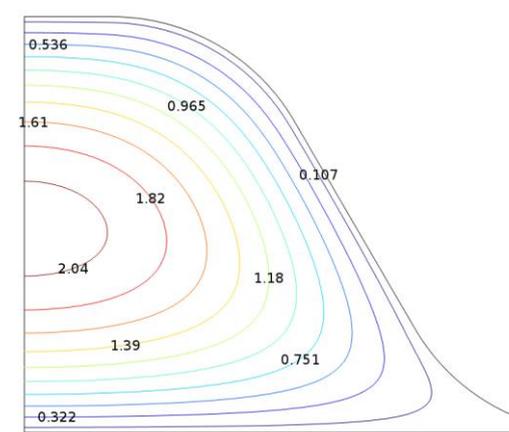
β = 0.5

Figure 6 Dimensionless (local velocities divided by the mean axial velocity) iso-velocity profiles across trapezoidal ducts for different β values for a given α (1) and θ (60°).
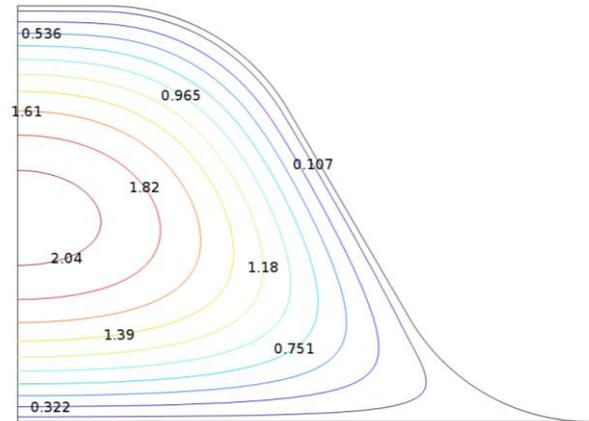
α = 0.5

α = 1
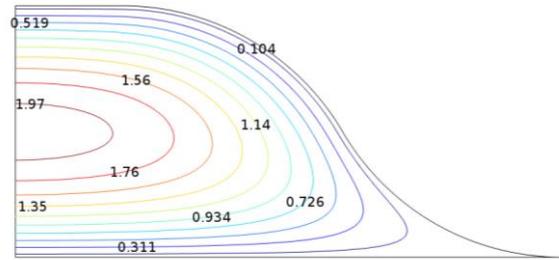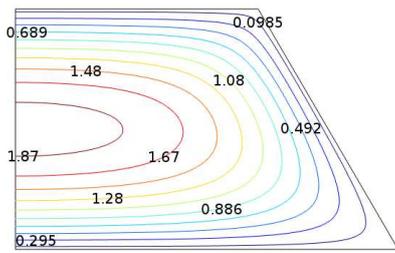
α = 2

1   **Figure 7 Dimensionless (local velocities divided by the mean axial velocity) iso-velocity**
2   **profiles across trapezoidal ducts for different α values (0.5, 1 and 2) with a given θ (60°)**
3   **and two β values: zero (left) and 0.5 (right).**
4

θ = 45°

θ = 60°

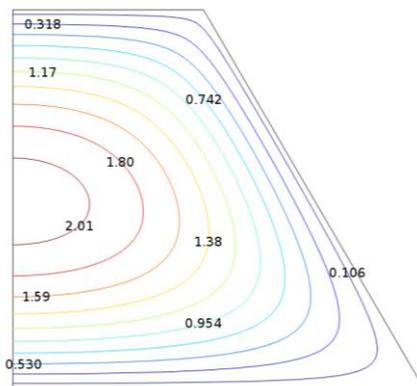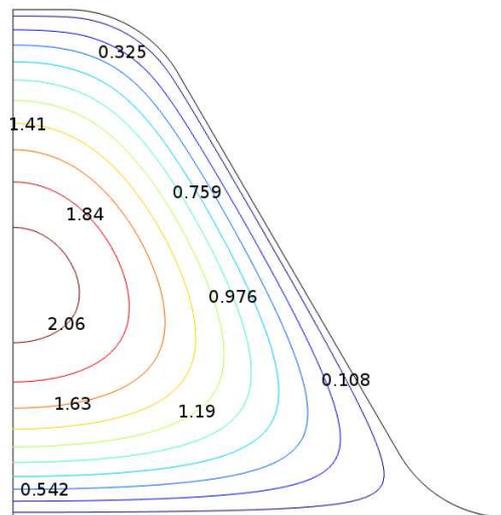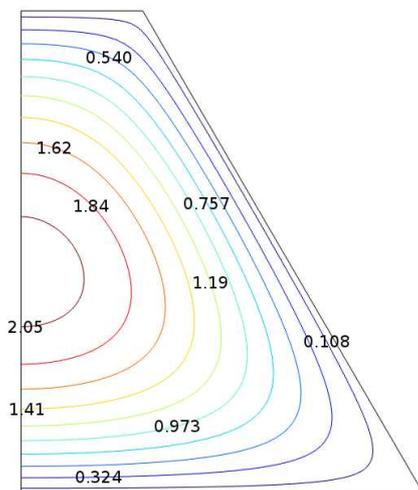**θ = 75°**
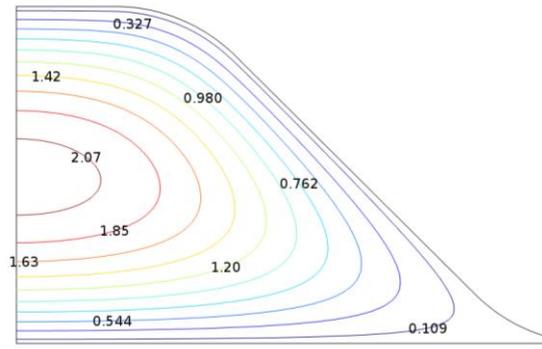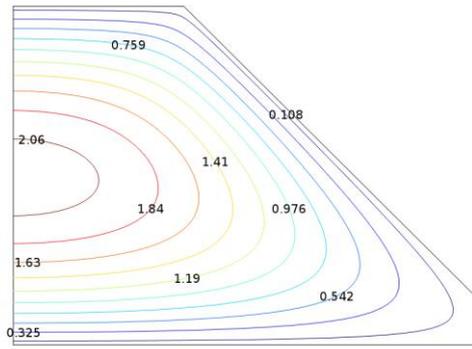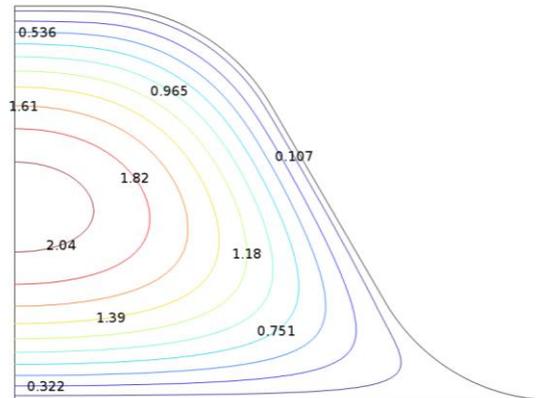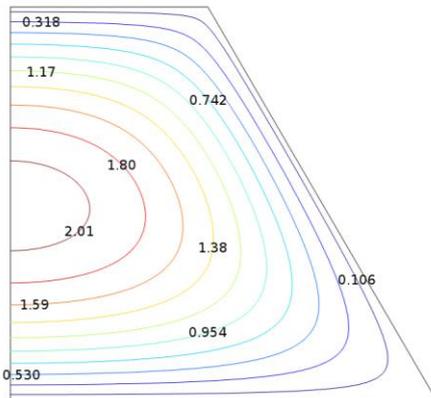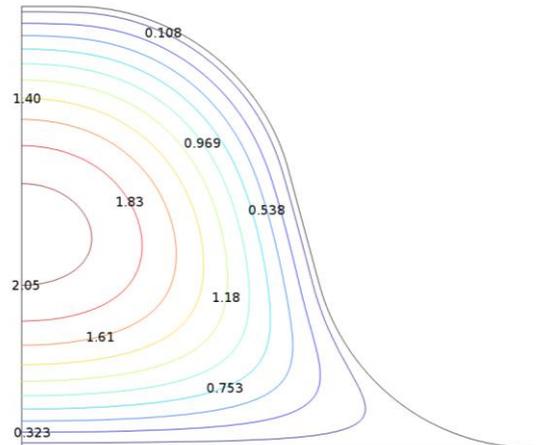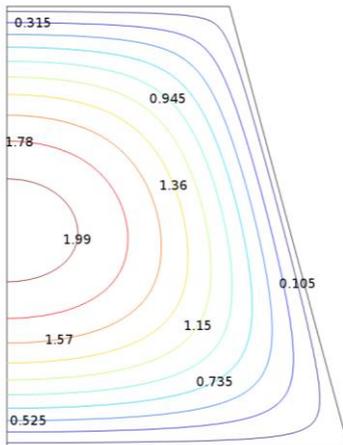
Figure 8 Dimensionless (local velocities divided by the mean axial velocity) iso-velocity profiles across trapezoidal ducts for different *θ* values (45, 60 and 75°) with a given *α* (1) and two β values: zero (left) and 0.5 (right).

1
2
3
4
5
6
7
8
9
10
11
12
13
14
15
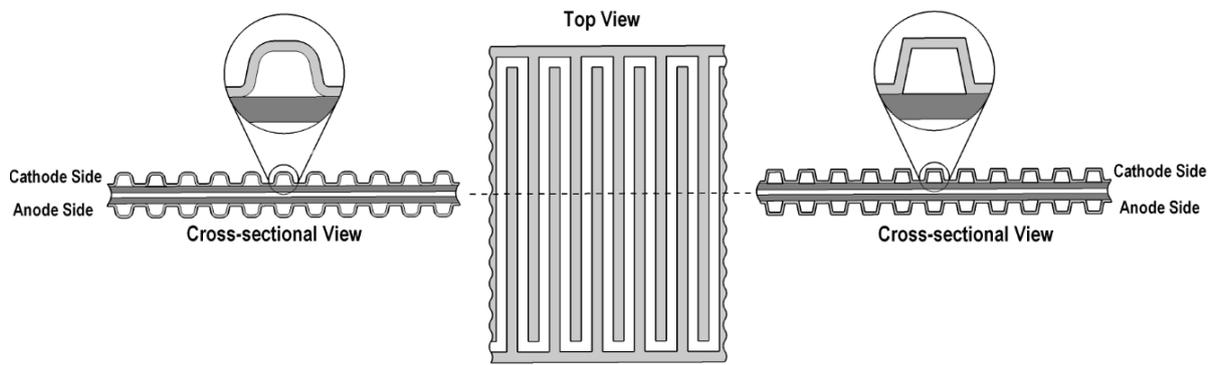
Figure 9 Top view for a serpentine flow channel. Cross-sectional views show the trapezoidal channels with rounded (left) and sharp (right) corners.

16
17
18
19

1

2

3

4

5

6

7

8

9

10 **Table 1 Change of fRe with mesh size for a trapezoidal cross-section with $\alpha = 1$, $\beta = 0.5$**
11 **and $\theta = 60°$. Note that COMSOL Multiphysics® automatically generates the mesh upon**
12 **selecting the predefined mesh designations (e.g. ~ 40 elements for 'Extremely Coarse'**
13 **designation and ~ 11350 elements for 'Extremely Fine' designation).**

Approximate number of elements	fRe
40	10.617714
85	10.589708
160	10.576060
300	10.574476
440	10.574165
900	10.574024
2900	10.574003
11350	10.574000

14

Table 2 The Poiseuille number (fRe), the incremental pressure drop ($K(\infty)$), the dimensionless hydrodynamic entrance length (L_{hy}^*) and the ratio of the maximum axial velocity to the mean axial velocity (u_{max}/u_m) for trapezoidal ducts as they change with the sidewall angle (θ), the ratio α and the ratio β.

	(fRe)														
	$\theta = 90°$			$\theta = 75°$			$\theta = 60°$			$\theta = 45°$			$\theta = 30°$		
	$\alpha = 0.5$	$\alpha = 1$	$\alpha = 2$	$\alpha = 0.5$	$\alpha = 1$	$\alpha = 2$	$\alpha = 0.5$	$\alpha = 1$	$\alpha = 2$	$\alpha = 0.5$	$\alpha = 1$	$\alpha = 2$	$\alpha = 0.5$	$\alpha = 1$	$\alpha = 2$
$\beta = 0.0$	15.548	14.227	15.548	15.804	14.252	14.340	15.692	14.151	13.805	15.212	13.822	13.369	14.346	13.255	12.870
$\beta = 0.1$	13.457	12.741	14.432	13.945	13.007	13.518	14.239	13.230	13.243	14.246	13.242	13.035	13.850	12.974	12.716
$\beta = 0.2$	11.930	11.534	13.457	12.520	11.958	12.775	13.046	12.416	12.719	13.397	12.706	12.716	13.387	12.704	12.566
$\beta = 0.3$	-	10.599	12.623	-	11.099	12.111	12.091	11.707	12.234	12.658	12.214	12.411	12.957	12.445	12.419
$\beta = 0.4$	-	9.9057	11.921	-	10.411	11.524	11.337	11.096	11.787	12.020	11.763	12.121	12.557	12.198	12.275
$\beta = 0.5$	-	9.4172	11.330	-	9.8747	11.008	10.750	10.574	11.376	11.471	11.353	11.845	12.187	11.961	12.135
	($K(\infty)$)														
$\beta = 0.0$	1.3829	1.5515	1.3829	1.3544	1.5634	1.5686	1.3785	1.6183	1.6872	1.4660	1.7405	1.8491	1.6618	1.9719	2.1085
$\beta = 0.1$	1.3936	1.5549	1.3841	1.3626	1.5657	1.5693	1.3830	1.6195	1.6875	1.4680	1.7410	1.8492	1.6624	1.9720	2.1085
$\beta = 0.2$	1.4537	1.5783	1.3936	1.4058	1.5799	1.5738	1.4056	1.6261	1.6893	1.4768	1.7433	1.8498	1.6646	1.9725	2.1086
$\beta = 0.3$	-	1.6280	1.4168	-	1.6104	1.5848	1.4503	1.6402	1.6934	1.4943	1.7481	1.8510	1.6688	1.9735	2.1088
$\beta = 0.4$	-	1.6971	1.4551	-	1.6555	1.6035	1.5157	1.6620	1.7003	1.5207	1.7556	1.8530	1.6751	1.9749	2.1091
$\beta = 0.5$	-	1.7747	1.5078	-	1.7115	1.6301	1.5984	1.6911	1.7102	1.5559	1.7657	1.8558	1.6835	1.9769	2.1095
	(L_{hy}^*)														
$\beta = 0.0$	0.025475	0.032381	0.025475	0.024037	0.032347	0.032650	0.023882	0.033094	0.035965	0.025112	0.035463	0.039957	0.028729	0.040823	0.046868
$\beta = 0.1$	0.029508	0.036177	0.027450	0.027311	0.035456	0.034641	0.026365	0.035408	0.037494	0.026842	0.037020	0.040979	0.029771	0.041709	0.047434
$\beta = 0.2$	0.034032	0.040134	0.029508	0.030970	0.038677	0.036689	0.029080	0.037786	0.039051	0.028689	0.038608	0.042010	0.030855	0.042604	0.048002
$\beta = 0.3$	-	0.044213	0.031685	-	0.041980	0.038798	0.032149	0.040219	0.040631	0.030694	0.040223	0.043048	0.031993	0.043507	0.048572
$\beta = 0.4$	-	0.048338	0.034039	-	0.045324	0.040971	0.035666	0.042696	0.042230	0.032892	0.041864	0.044091	0.033192	0.044419	0.049138
$\beta = 0.5$	-	0.052364	0.036633	-	0.048673	0.043215	0.039667	0.045209	0.043846	0.035307	0.043528	0.045139	0.034458	0.045337	0.049707
	(u_{max}/u_m)														

β = 0.0	1.9918	2.0963	1.9918	1.9682	2.0994	2.1075	1.9691	2.1194	2.1618	1.9985	2.1682	2.2329	2.0762	2.2664	2.3497
β = 0.1	1.9955	2.0964	1.9918	1.9713	2.0995	2.1075	1.9710	2.1198	2.1619	1.9994	2.1684	2.2329	2.0765	2.2664	2.3497
β = 0.2	2.0193	2.0973	1.9922	1.9891	2.1001	2.1077	1.9807	2.1220	2.1624	2.0035	2.1692	2.2331	2.0777	2.2666	2.3497
β = 0.3	-	2.0999	1.9933	-	2.1018	2.1082	2.0013	2.1269	2.1637	2.0121	2.1710	2.2334	2.0801	2.2670	2.3498
β = 0.4	-	2.1047	1.9955	-	2.1048	2.1092	2.0330	2.1347	2.1660	2.0254	2.1738	2.2340	2.0838	2.2676	2.3498
β = 0.5	-	2.1121	1.9990	-	2.1092	2.1107	2.0746	2.1455	2.1692	2.0435	2.1777	2.2348	2.0888	2.2685	2.3499

1

2
3
4

Table 3 The geometrical properties of the flow channel and the density and the viscosity of the flowing gases in the cathodic (air) and the anodic (hydrogen) channels.

Parameter	Value
Length of upper base of channel (a)	1 mm
Height of channel (h)	1 mm
Sidewall angle (θ)	60°
Radius of fillet (r)	0 mm (Case 1); 0.5 mm (Case 2)
Density of air	1.20 kg m^{-3}
Density of hydrogen	0.09 kg m^{-3}
Viscosity of air	1.81×10^{-5} Pa.s
Viscosity of hydrogen	0.88×10^{-5} Pa.s

Table 4 The physical and the geometrical parameters required to calculate the pressure drop (ΔP), the hydrodynamic entrance length (L_{hy}) and the maximum axial velocity (u_{max}).

	$\beta = 0$		$\beta = 0.5$	
	Cathode	**Anode**	**Cathode**	**Anode**
Cross-section area (A)	1.58 mm^2			
Mean axial velocity (u_m) *	19.0 m s^{-1}	8.0 m s^{-1}	19.0 m s^{-1}	8.0 m s^{-1}
Perimeter (Γ)	5.46 mm		6.40 mm	
Hydraulic diameter (D_h)	1.15 mm		0.99 mm	
Reynolds number (Re)	1456	94	1242	80
Poiseuille number (fRe)	14.151		10.574	
Incremental pressure drop ($K(\infty)$)	1.6183		1.6911	
Dimensionless hydrodynamic entrance length (L_{hy}^*)	0.033094		0.045209	
Maximum axial velocity to mean axial velocity (u_{max}/u_m)	2.1194		2.1455	

* Calculated by dividing flow rates mentioned at the start of this section by the cross-sectional area of the channel (A).

Table 5 The pressure drop (ΔP), its breakdown into ΔP_{fd} and ΔP_{df}, the hydrodynamic entrance length (L_{hy}) and the maximum axial velocity (u_{max}) for the cathode and the anode sides of the fuel cell with either sharp ($\beta = 0$) or rounded ($\beta = 0.5$) corners.

	$\beta = 0$		$\beta = 0.5$	
	Cathode	**Anode**	**Cathode**	**Anode**
Pressure drop (ΔP)	22.274 kPa	4.481 kPa	22.866 kPa	4.599 kPa
Fully developed flow region related pressure drop (ΔP_{fd})	21.922 kPa	4.477 kPa	22.499 kPa	4.594 kPa
Developing flow region related pressure drop (ΔP_{df})	0.351 kPa	0.0046 kPa	0.367 kPa	0.0049 kPa
Hydrodynamic entrance length (L_{hy})	55.64 mm	3.60 mm	55.34 mm	3.59 mm
Maximum axial velocity (u_{max})	40.3 m s^{-1}	16.9 m s^{-1}	40.8 m s^{-1}	17.1 m s^{-1}